December 1991 TAO, Vol.2, No.4, 355-374

Observational Study of a Microburst-Producing Storm
Part IV: Fine Scale Analysis

YEONG-JER LIN[1] AND BRADLEY T. REGAN [2] ROBERT W. PASKEN [3]

(Received 30 June 1991; Revised 4 December 1991)

ABSTRACT

Data are presented for several microburst events as they occurred on 5 August 1982 at 1845 LST. The kinematic, dyamic, and thermodynamic structures of these storms were investigated using dual-Doppler data collected during the JAWS project. Fields of storm-relative wind and reflectivity were derived using the objective analysis scheme with 0.25 *km* horizontal grid spacing and compared with a previous study which used 0.5 *km* horizontal grid spacing. There were five layers in the vertical ranging from 0.25 to 1.25 *km*. Vertical velocities were calculated from the anelastic continuity equation by integrating upward from the surface to the top of the atmospheric boundary layer. The thermodynamic retrieval method was employed to retrieve fields of perturbation pressure and temperature from the Doppler derived winds using the three momentum equations.

Results show that several features undetected at the 0.5 *km* grid scale become apparent at the 0.25 *km* grid. Further, most features observed in this study become strikingly more apparent both in magnitude and appearance than the earlier study using 0.5 *km* horizontal grid spacing. The quality and resolution of dual-Doppler derived winds are critical to the success of a thermodynamic retrieval technique.

1. INTRODUCTION

In Part I of this study, Lin *et al.* (1991) investigated some structural features of a multiple microburst-producing storm, the 5 August 1982 case, in detail using the JAWS (Joint Airport Weather Studies) dual-Doppler data with 0.5 *km* horizontal grid spacing. Results obtained were then compared to those for the 14 July 1982 case in Part II (Lin and Coover, 1991) of this study

---

[1] *Department of Earth and Atmospheric Sciences, Saint Louis University, U. S. A.*

[2] *Present Affiliation: Air Weather Service, U. S. Air Force*

[3] *Department of Mathematics, Parks College of Saint Louis University, U. S. A.*

using the 0.5 *km* grid distance. Vorticity distributions and budgets of these two microburst-producing storms were examined in Part III of the study by Lin and Lapointe (1991) using the Doppler derived winds obtained in Parts I and II mentioned above.

With the aid of JAWS Doppler data, many microburst studies with emphasis on their kinematic structure were reported in the literature; for example, see studies by Wilson *et al.* (1984), Elmore *et al.* (1986), Hjelmfelt (1988), Lee *et al.* (1988), Kessinger *et al.* (1988) and others. The kinematic structure of the 5 August 1982 case was studies by Elmore *et al.* (1986) using the reduced domain (4.5 *km* × 4.5 *km*) centered at microburst M1. The objective analysis employed was the Cressman (1959) interpolation scheme with an influence radius equal to the grid spacing of 150 *m*. They used the 150 *m* horizontal grid spacing to calculate fields of convergence/divergence and vertical velocity starting from the lowest level near 50 *m* AGL (above ground level). Results showed that strong downward motion occurred inside the microburst.

In the kinematic study of a microburst, only the first derivative in velocity is required to compute vertical shears, fields of convergence/divergence, vorticity and vertical velocity. For this reason, researchers were able to choose much smaller grid spacing, say 250 *m* or less, to compute those kinematic quantities. Hence small-scale features associated with microbursts in the atmospheric boundary layer (ABL) can be resolved, see studies by Wilson *et al.* (1984), Elmore *et al.* (1986), Hjelmfelt (1988), etc. Conversely, in the dynamic and thermodynamic study of a microburst-producing storm using a thermodynamic retrieval method, e.g., Lin *et al.* (1991), Lin and Coover (1991) and others, first, second and third derivatives in velocity are required to retrieve fields of perturbation pressure and temperature. Consequently, higher quality wind data are needed for the dynamic and thermodynamic study of a microburst storm. This can be achieved by suppressing smaller scale perturbations in the wind field via smoothing or filtering.

As depicted in Part I of this study, our study employed a Barnes (1973) distance-dependent weighting function (instead of a Cressman type weighting)[1] with a 1.75 *km* scan radius to interpolate data on a grid. The 0.5 *km* horizontal grid spacing was chosen to be compatible with a 1.75 *km* scan radius. Hence, small-scale features with wavelength < 3 *km* were not resolved in Parts I, II and III of this study. It is of interest to investigate the fine-scale structure of a microburst-producing storm, via a thermodynamic retrieval technique, by reducing the horizontal grid spacing to 0.25 *km* with a scan radius of 0.875 *km*.

---

[1] *The advantage of using Barnes' scheme over Cressman's scheme was discussed in the study by Koch et al. [1983]*

In this way, mesoscale features with wavelength > 1.5 *km* can be adequately resolved using the JAWS data mentioned previously.

The purpose of this study in Part IV is to investigate the kinematic, dynamic and thermodynamic properties of the same microburst-producing storm, studied in detail in Part I of this study, using a 0.25 *km* grid spacing in both horizontal and vertical directions. This multiple microburst-producing storm occurred on 5 August 1982 near Denver, Colorado. In addition to studying the fine-scale structure of the storm, a cross comparison will then be made between the current study using to 0.25 *km* resolution and the previous study using the 0.5 *km* resolution. Throughout such a comparison, the structure and internal dynamics of a multiple microburst-producing storm in the ABL can be further understood.

2. DATA AND ANALYSIS PROCEDURES

The synoptic condition for the 5 August 1982 case (the complex case) was presented in Section 2 of Part I. Briefly, the Denver sounding released at 1800 MDT (mountain daylight time), see Figure 2 in Part I, dispalayed a well mixed boundary layer extending to 1.5 *km* AGL. The convective condensation level was located at 650 *mb* with a surface temperature of $30^\circ C$. Also, moist conditions prevailed aloft throughout the depth of $4 \sim 7$ *km*. An average mixing ratio value of 6.5 $g\ kg^{-1}$ existed within the 3 *km* thick moist layer. Note the lack of mid-level dry air common to most upper/high plains soundings. The height of the $0^\circ C$ wet bulb temperature is 2.8 *km* AGL, indicative of a hail producing storm.

We used the data analysis and reduction procedures, outlined in Part I of this study (Lin *et al*., 1991), to process the dual-Doppler data obtained from CP-3 and CP-4. These data were strictly checked to meet the prespecified criterion, i.e., values of reflectivity (Z) must be larger than 5 dBZ. Folded data were collected and ground clutters were removed. Only those data with signal-to noise ratio values greater than or equal to 10 dB were accepted for analysis in each slab. All variables within a slab were interpolated onto horizontal grids (42×48) with a grid spacing of 0.25 *km* using a 0.875 *km* scan radius. There were five equally spaced analysis levels in the vertical ranging from 0.25 to 1.25 *km*.

3. METHODOLOGY

We employed the method suggested by Armijo (1969) to derive the horizontal wind components from two radial velocity equations, the anelastic continuity equation and an empirical formula of terminal fall speed. Vertical velocities were computed from the anelastic continuity equation by integrating upward from the surface assuming zero vertical velocity at the surface. Once the three-dimensional winds were obtained, fields of deviation perturbation pressure and temperature were retrieved from the Doppler derived winds using the three momentum equations (Gal-Chen, 1978). These fields were subjected to momentum checks (E_r) to determine the level of confidence before interpretation. For detail, see Part I of this study. Values of E_r vary from 0.21 to 0.39 with the volume mean of 0.34.

4. DISCUSSION OF RESULTS

As noted earlier in Section 1, the employment of smaller grid (0.25 *km*) should provide finer resolution of those events captured at the times of investigation. Analyses are conducted by dissecting five horizontal levels separated at 0.25 *km* intervals for the structural features of those storms present. Indeed, storm features resolved at the 0.5 *km* grid analysis are significantly more pronounced than those at the 0.25 *km* grid analysis and will be discussed later. Additional features of interest also become apparent at the refined scale. Fields of storm-relative wind, reflectivity, vertical velocity along with perturbation pressure and temperature are presented below with distances in kilometers relative to the CP-2 radar. In an effort to show the fine-scale structure of motion, the scale of wind vectors displayed at the 0.25 *km* analyses (Figures 1a, 2a, 6a,

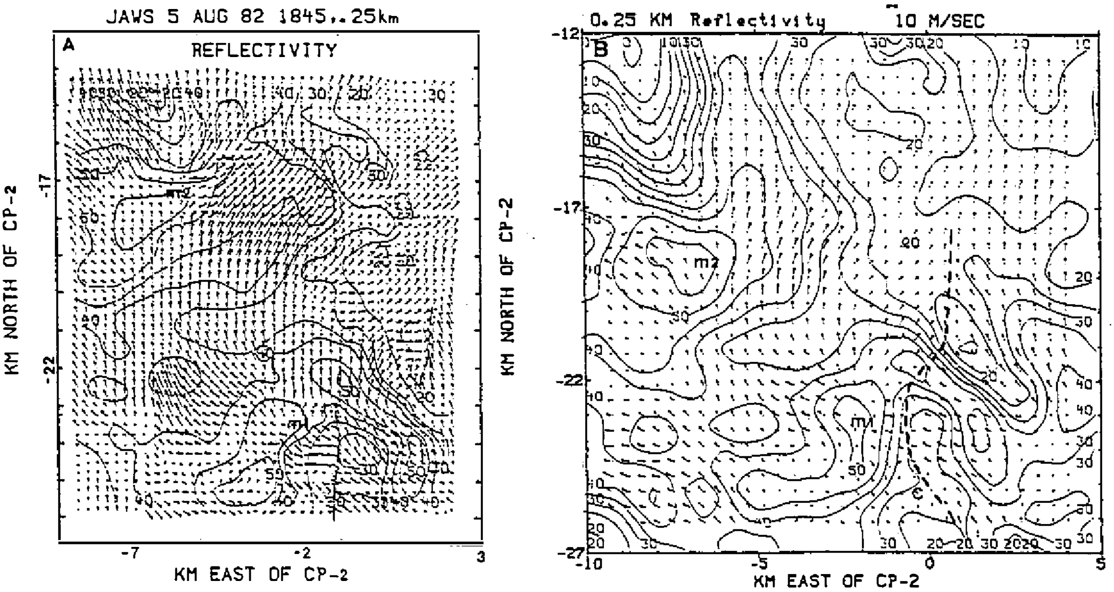

Fig. 1. Horizontal winds with reflectivity contours superimposed at 0.25 *km* AGL for 1845 MDT 5 August 1982 using (a) 0.25 and (b) 0.5 *km* grid spacing. Distances are in kilometers from the CP-2 radar. Contour interval is 5 *dBZ*. Locations of microbursts (*M*) and gust fronts (dashed line) are indicated.

7a and 11a) is exaggerated by a factor of 2 as compared to that at the 0.5 *km* analysis.

4.1 Plan View at 0.25 *km*

Figure 1 displays the plain view of the horizontal wind and reflectivity field using both 0.25 and 0.5 *km* horizontal grid spacings. Similar to the 0.5 *km* horizontal grid spacing analysis (Figure 1b), the 0.25 *km* analysis (Figure 1a) also reveals that two microburst events are visible (M1 and M2) and found to be situated near or within the areas of highest reflectivity with values of 45 *dBZ* or greater. The dominant microburst feature, M1, is located at ($x = -2$, $y = -23.5$). Microburst M2 is located northwest of M1 near (−6, −17.5). The second microburst, M2, is strikingly more visible than as presented at the 0.5 *km* analysis (see Figure 1b). Hence, its center is better defined for 0.25 *km* resolution than that for 0.5 *km* resolution. Notice the disagreement in location for M2 between the two analyses. This is attributed to the fact that at the 0.5 *km* analysis (Figure 1b), M2 does not have an apparent diverging outflow from its center, especially in the southeast part of M2. As a result, the location of M2 as shown in Figure 1b for 0.5 *km* resolution is not as accurate as that shown in Figure 1a for 0.25 *km* resolution. This point must be kept in mind when the two cases are compared.

The environmental flow at this level is from 220° at $3 \sim 4\ m\ s^{-1}$. A gust front, indicated by the dashed line, is noted at the southeast portion of the grid, which is caused by collision between the M1 eastward divergent outflow boundary and the cyclonic circulation (inflow) just south of the shear line (Figure 1a). An additional cyclonic circulation is found to appear to the west-southwest of M1 near (−6.5, −24), a feature which goes unnoticed at the 0.5 *km* grid datum (Figure 1b). The maximum divergence associated with M2 is displaced downwind of its highest reflectivity core and largely due to a coupling between the environmental wind and the M1 outflow boundary.

4.2 Plan View at 0.5 *km*

At 0.5 *km* (Figure 2), both microbursts M1 and M2 are active, though slightly less pronounced than at 0.25 *km*, in areas of high reflectivity. Two cyclonic circulations within the vicinity of M1, one located at (−0.5, −25.5) on the southern edge of the gust front and the other due west in the southwestern portion of the grid domain near (−6.5, −24), remain present and well defined (Figure 2a). However, these circulations are not clearly shown in the 0.5 *km* horizontal grid spacing (Figure 2b).

The vertical velocity field (Figure 3) indicates values of −3 and $-2\ m\ s^{-1}$ vertical motion for microbursts M1 and M2, respectively. These values are larger than those of 0.5 *km* grid resolution (see Figure 6a in Part I). Note that

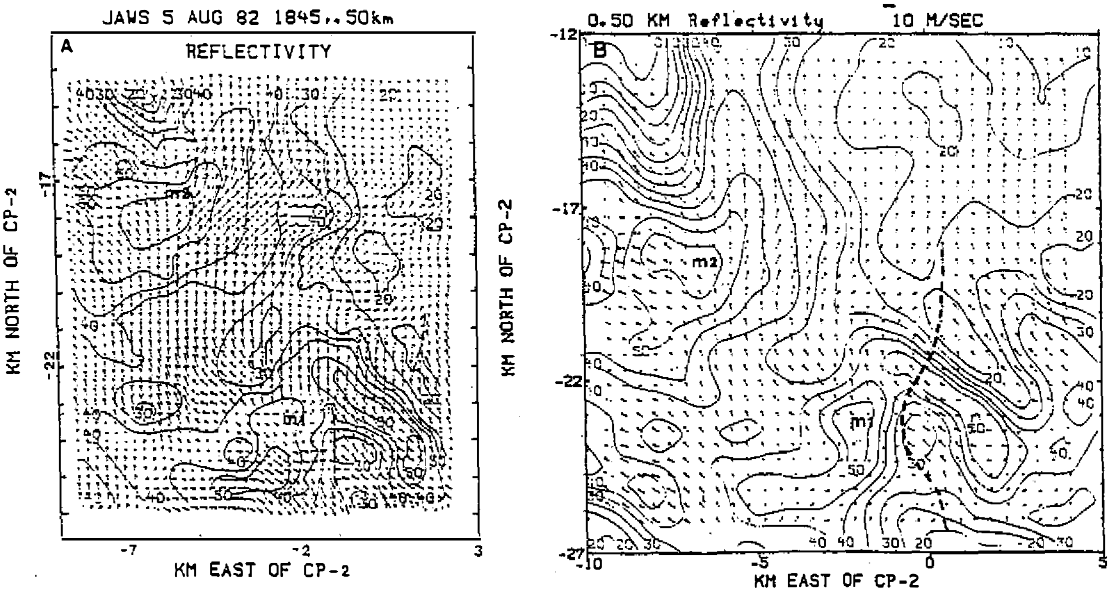

Fig. 2. As in Figure 1 except for 0.5 *km* AGL.

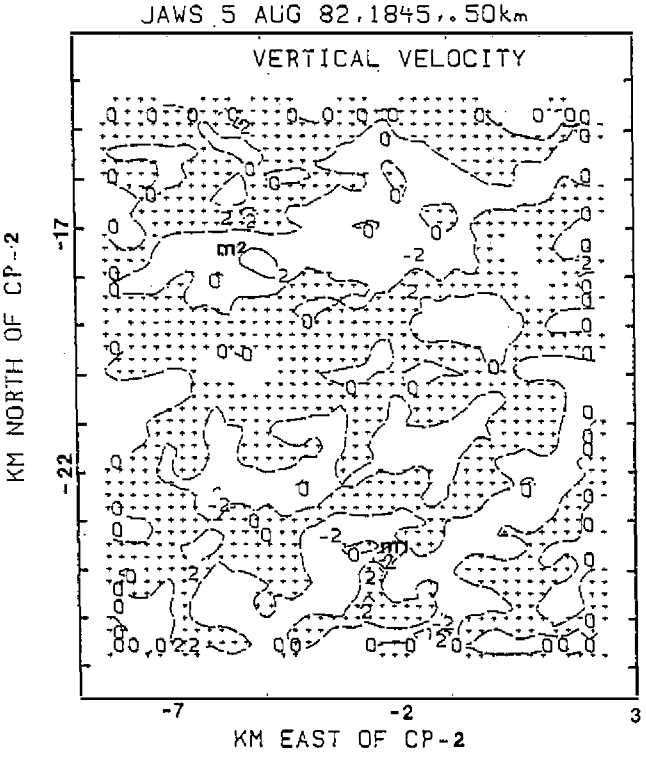

Fig. 3. Horizontal destribution of vertical velocity (w) at 0.5 *km* AGL for 1845 MDT 5 August 1982 using 0.25 *km* grid spacing. Contour interval is 2 $m\ s^{-1}$ with positive values shaded. Locations of microburst M1 and M2 are indicated.

the vertical velocity field clearly identifies M1 and M2 as areas of sinking motion. A ring of upward motion is observed to flank both microburst events. Updraft speeds vary from $1 \sim 2\ m\ s^{-1}$ in the vicinity of microbursts M1 and M2. The cyclonic circulation due west of M1 near (−6.5, −24) carries an updraft value of $2\ m\ s^{-1}$. The vertical velocity field thus provides credence for all features discussed. Upon examining those parameters discovered thus far, one is led to conclude that a correlation should exist between the vertical velocity and the pressure fields.

The perturbation pressure pattern at this level (Figure 4) displays each microburst event as a relatively high pressure anomaly. This feature is more clearly seen at 0.25 *km* (not shown). Low pressure may be found along the gust front and generally surrounds the microburst high pressure regions. The temperature field (Figure 5) is less amplified, but still indicates that each microburst is typified by a cold-core anomaly. A cold temperature value of −1 to $-2^\circ C$ accompanies each microburst event with a warm pool of air ($1 \sim 2^\circ C$) existent within the central grid domain, consistent with the 0.25 *km* level and area of strong updrafts (not shown). Additionally, the cyclonic circulation on the gust front features a relatively cooler region than 0.25 *km* as upward vertical motion increases, thereby cooling the unsaturated inflow air by dry adiabatic expansion. A cool temperature perturbation of $-2^\circ C$, located at (−1, −25.5), corresponds to the gust front cyclone (Figure 2a), while a value of $-1^\circ C$ accompanies the cyclone in the southwest of the domain near (−6.5, −24), indicative of dry adiabatic expansion associated with its $2\ m\ s^{-1}$ updraft. Note that the temperature pattern depicted in Figure 5 is more pronounced than that presented in Part I (Figure 9a) with 0.5 *km* grid resolution. Cooler temperatures are observed in the M1 and M2 domains in both cases. However, relative warming found in the areas south of M1 and M2 for 0.25 *km* resolution (Figure 5) is different from that observed in the 0.5 *km* case. Such warming is associated with upward motion is those areas (see Figures 3 and 5 for comparison).

4.3 Plan View at 0.75 *km*

Structural features are seen to undergo a transition at the 0.75 *km* level as attested by the horizontal wind field (Figure 6a). The environmental flow becomes more dominant in the horizontal plane as the entire wind field for the grid is predominantly southeast or southerly with little horizontal eddy motion. The environmental flow actually begins to dominate the microburst core regions persisting into the 50 *dBZ* contour. But the M2 outflow boundary becomes replaced by cyclonic motion. Structural changes associated with M1 are less pronounced, although cyclonic turning of the wind becomes apparent to its north. The gust front is not well defined at this level, but the cyclonic gyration to the south of its presumed position near (−1, −25.5) remains. This feature is

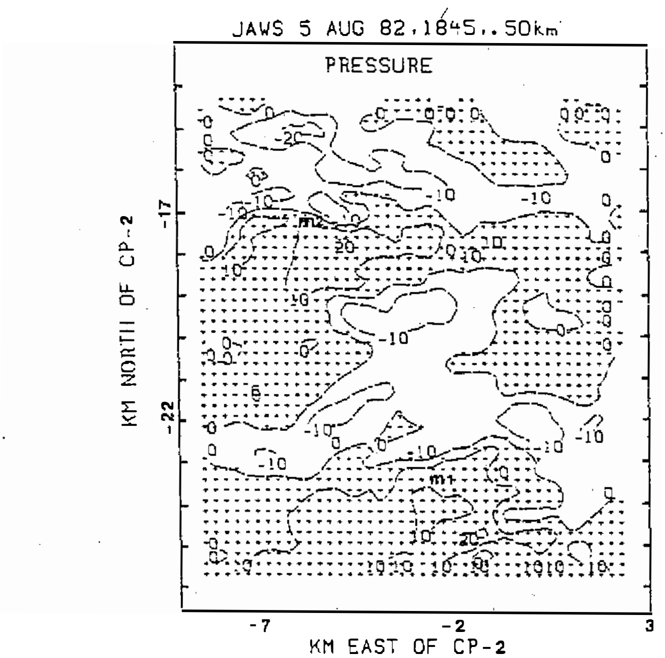

Fig. 4. As in Figure 3 except for deviation perturbation pressure (P'_d). Contour interval is 10 Pa (0.1 mb) with positive values shaded.

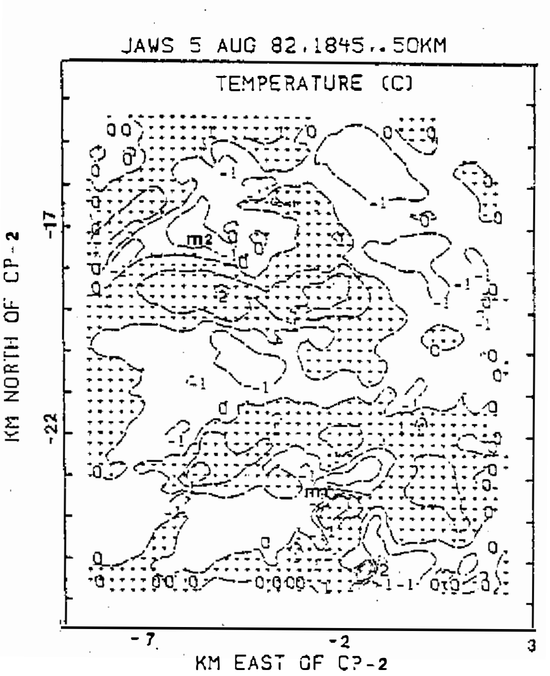

Fig. 5. As in Figure 3 except for deviation perturbation temperature (T'_{vd}). Contour interval is $1°C$ with positive values shaded.

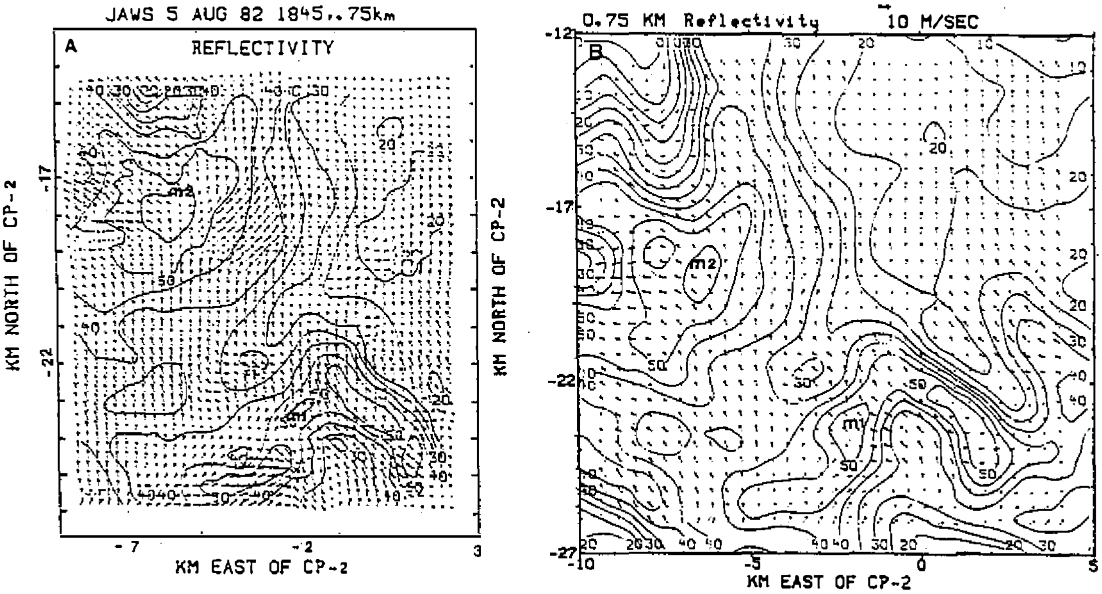

Fig. 6. As in Figure 1 except for 0.75 *km* AGL.

not clearly seen in Figure 6b with 0.5 *km* resolution. The cyclonic circulation due west of M1 has completely vanished being over run by the environmental flow. Thus, it appears that this cyclonic circulation extends only to 0.75 *km* in depth. Each microburst remains intact with respect to vertical velocity and carries values of $-4\ m\ s^{-1}$ (not shown). Therefore, vertical velocity continues to verify the presence of the microbursts, but it becomes clear that this level is one of transitional change of storm composition. The 0.75 *km* level may thus be equated to the level of non-divergence for these microburst events. The microburst downdraft does not decelerate greatly due to the effect of the earth's surface, nor is it at a level where mass originates for downward transport since little entrainment occurs into the level nor transport out of the downdraft. The level thus represents an active channel where mass collected from above passes down through the layer to levels below where it may be distributed by horizontal divergence.

The winds at this level are seen to blow parallel to the reflectivity contours to the northeast of M2 and to the southeast of the cyclonic circulation. Indications are that strong outflow of precipitation cooled air from the high reflectivity core, which occurred at lower levels, is not taking place. Entrainment of dry environmental air from flow towards higher reflectivity values is likewise absent. Therefore, dry air entrainment of environmental air should be occurring at upper levels. Inspection of those levels aloft will undoubtedly provide clues into the structural properties of microburst phenomena.

4.4 Plan View at 1 *km*

Examination of the 1 *km* level (Figure 7a) indicates that definite changes have taken place as opposed to the lower levels. The only feature which remains unchanged is the cyclonic circulation south of the presumed surface gust front location near (−1.5, −25.5). However, this cyclonic feature is not clearly observed in Figure 7b with 0.5 *km* resolution. Strong cyclonic motion occurs for both microbursts to the north of their central core regions. Additionally, the strong winds associated with the central grid updrafts found at lower levels are much less amplified. Dry air entrainment begins to occur at 1 *km*, thereby feeding the microburst events, as evident by an increase in the crossing angle flow of the environmental air from low to high reflectivity cores associated with the descending precipitation shaft. Additionally, cyclonic curvature becomes established on the north sides of M1 and M2. Vivid finger like protrusions accompany each microburst event. A finger like appendage is noted in the reflectivity pocket southwest of M1, an area of 50 *dBZ*, which curls counter-clockwise up the grid and back towards M1. Another finger like projection extends down the grid from the extreme northwest corner of the grid, pointing at M2. These finger like appendages act as circulation feeders, which provide abundant tongues of dry environmental air for digestion into microburst core regions. Cyclonic flow around both microburst events is much broader and more pronounced than at lower levels. The cyclonic circulation to the west southwest of M1, found absent at 0.75 *km*, becomes reestablished at this level. A streamline analysis would

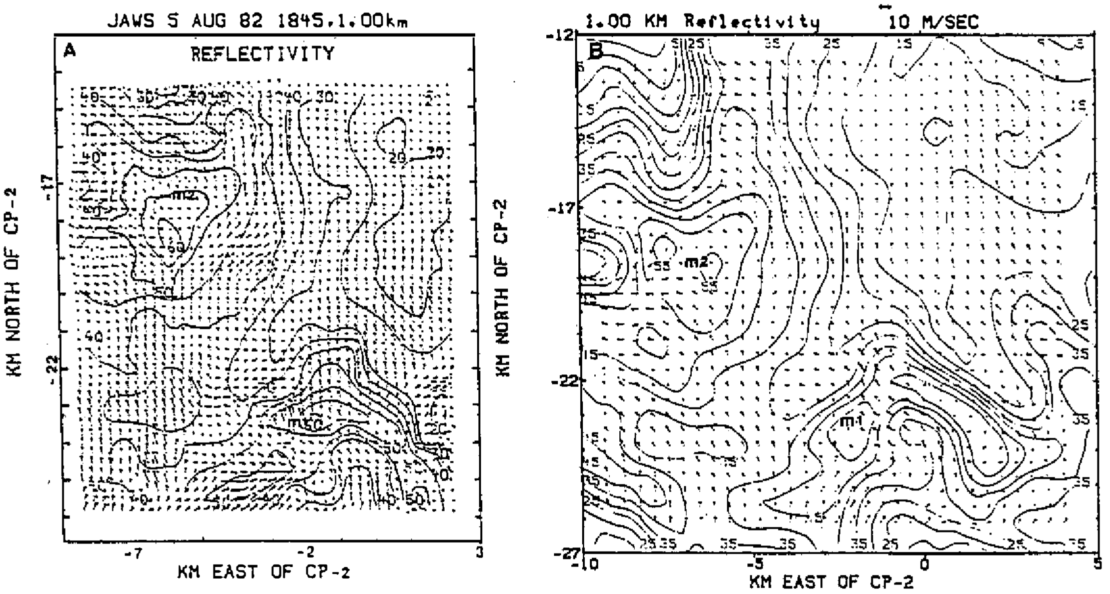

Fig. 7. As in Figure 1 except for 1 *km* AGL.

well diagram a confluent asymptote connecting the low pressure microburst regions; which is fed and driven by anticyclonic curvature in the central portion of the domain and just northwest of M1. Anticyclonic flow is also visible in the southeast portion of the domain.

The vertical velocity field (Figure 8) characterizes each microburst event with downdraft values of $-6\ m\ s^{-1}$. A semicircle of updraft values ($3\ m\ s^{-1}$) envelopes M2 on its northwestern edge, while updraft values encircling M1's northeastern edge are $6\ m\ s^{-1}$. The cyclonic gyre due west of M1 near (−3, −23.5) maintains a downdraft speed of $-6\ m\ s^{-1}$, but reduces to $-2\ m\ s^{-1}$ at 0.5 *km* (Figure 3). Speeds of $3 \sim 6\ m\ s^{-1}$ accompany the strong updrafts, consistent at all levels, within the central grid region. A strong updraft may also be found south of M1 near (−2.5, −25) with a speed of $6\ m\ s^{-1}$. Note that values of w presented in Figure 8 are, in general, $2 \sim 3$ times larger than those with 0.5 *km* resolution (see Figure 6b in Part I). This finding is reasonable, since the utilization of 0.25 *km* grid resolution is able to capture some features associated with fine-scale structure of a microburst-producing storm. As a result, both updrafts and downdrafts become stronger as depicted in Figure 8.

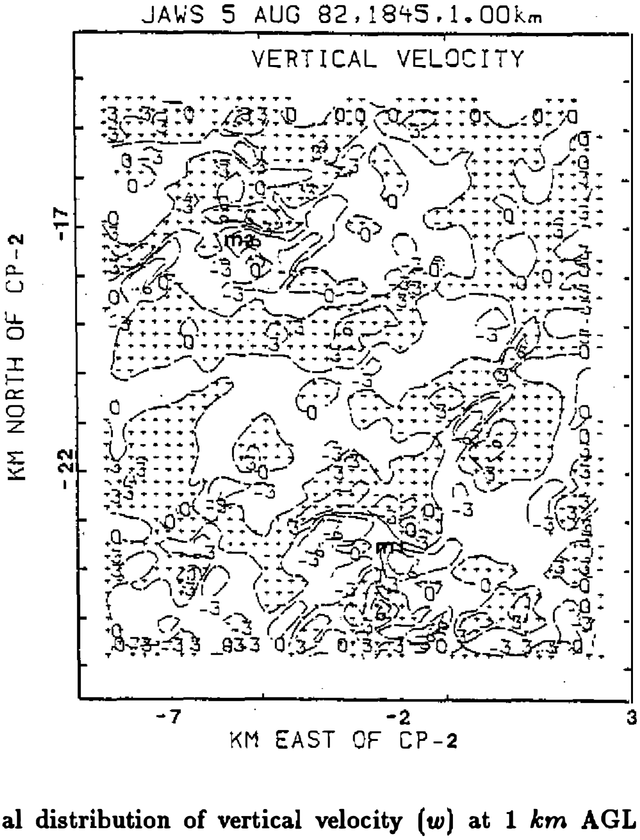

Fig. 8. Horizontal distribution of vertical velocity (w) at 1 *km* AGL for 1845 MDT 5 August 1982 using 0.25 *km* grid spacing. Contour interval is $3\ m\ s^{-1}$ with positive values shaded. Locations of microburst M1 and M2 are indicated.

Figure 9 displays the perturbation pressure pattern for this level where highest pressure is found near the southeast and northwest corners of the domain. The low pressure centers, located at (−3, −23.5) and (−1.5, −25.5), are found near the centers of cyclonic circulation mentioned previously. Mass flow, therefore, is toward the cyclonic center from the surrounding region not associated with the cyclonic gyre, analogous to sedimentary erosion at points of low terrain.

Updraft regions which flank each microburst event maintain high pressure anomalies between 0.1 and 0.2 *mb*. The cyclonic gyre west southwest of M1 near (−6.5, −25) has a −0.1 *mb* low pressure value with a similar high pressure value to its southwest.

The perturbation temperature field (Figure 10) exhibits warm-core anomalies for both microburst regions with surrounding cool air (−1 to −2° *C*). The cold anomalies are believed, in part, resultant from dry adiabatic expansion of the lower level environmental air being channeled aloft within updraft areas. Similarly, cold temperature anomaly values associated with M2 vary between −1 and −2° *C*. Temperatures along the supposed gust front location

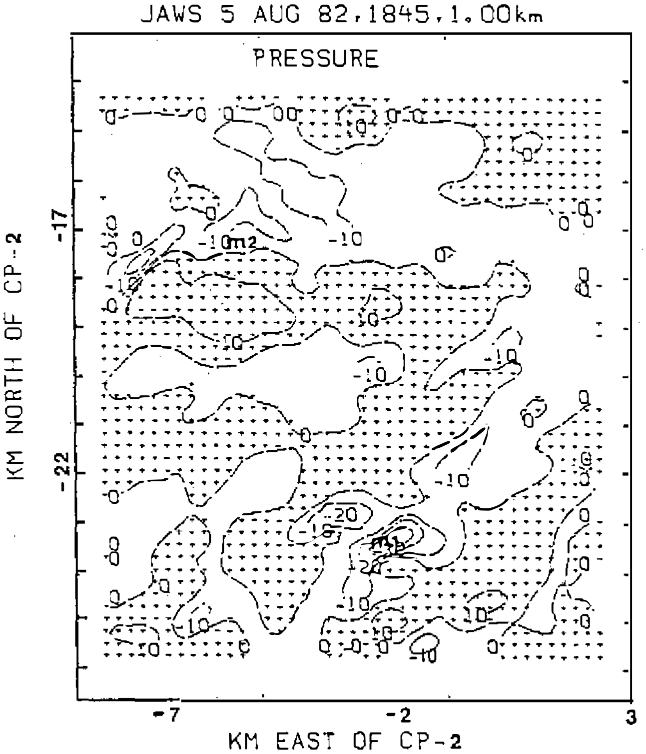

Fig. 9. As in Figure 8 except for deviation perturbation pressure (P_d'). Contour interval is 10 *Pa* (0.1 *mb*) with positive values shaded.

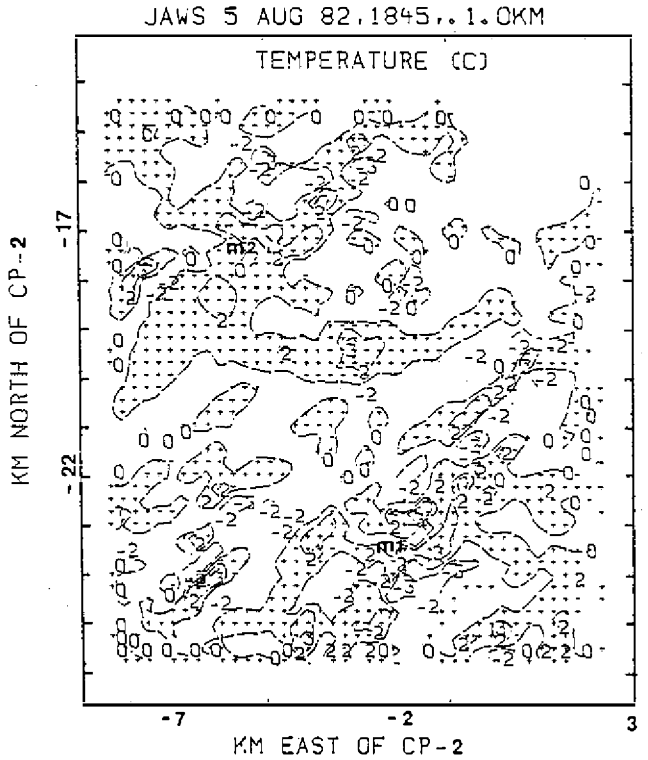

Fig. 10. As in Figure 8 except for deviation perturbation temperature (T'_{vd}). Contour interval is 1°C with positive values shaded.

remain neutral, while the cyclonic gyre west of M1 is also a cold core ($-2° C$). A warm anomaly ($2° C$) exists with the relatively warm, dry environmental air entrained into the system to the southeast of M1. Microburst M2 is assiciated with cooling on its north side with a warm anomaly noted within the southward flowing entrained environmental air. It is interesting to note that relatively warm temperature values exist aloft within each parent storm, but low temperature values occur at lower levels. The warm anomalies must be linked to compressional warming associated with rapid convergence and entrainment of environmental air being directed into the intense cyclonic circulation, which becomes subject to explosive descent as indicated by the vertical velocity field (Figure 8). Note that the warm anomalies quickly fade at 0.75 *km* and below, largely due to evaporating precipitation shafts which regain a foothold within the microburst structural domain. Furthermore, a warm anomaly dominates an area of low reflectivity and upward motion as indicated by the vertical velocity field (Figure 8) and may be associated with the outflow from the bow echo. The bow echo itself is warm-core but surrounded by cooler air, probably due to the entrainment process. Note the inflow of environmental air feeding into this feature from the southeast. As the warm environmental air becomes horizontally entrained, it maintains a warm anomaly due to slow rising and cooling until entering the major updraft. It does not encounter evaporative cooling until it enters the updraft and meets the surrounding saturated region of the updraft. Upon entering the main updraft, dry adiabatic ascent rapidly cools the region, thereby becoming a cold anomaly.

4.5 Plan View at 1.25 *km*

The flow field with reflectivity contours superimposed at 1.25 is shown in Figure 11. The finger like appendages discussed earlier are more numerous and tongue like in resemblance. The finger like appendages associated with the dry air intrusions are broader than 1 *km* and the crossing angle of environmental air toward the high reflectivity core increases to almost a perpendicular angle. Cyclonic turning of the wind occurs around both microbursts with pronounced cyclonic circulation visible around M1. Mass is thus noted to spiral inward prior to its descent within the microburst core. Two cyclonic circulations are evident at this level. One is located southwest of M1 near (−3.5, −24), and the other is to the southeast of M2 near (−5, −18.5). These two cyclonic circulations correspond to the misocyclones discussed in Parts I and III of this study. These two misocyclones are better resolved with 0.25 *km* grid resolution (Figure 11a) than those with 0.5 *km* resolution (Figure 11b). In addition, the 0.25 *km* grid provides much stronger reflectivities (up to 60 *dBZ*) in the microburst regions.

Inspection of Figure 11a further reveals that the anticyclonic flow visible

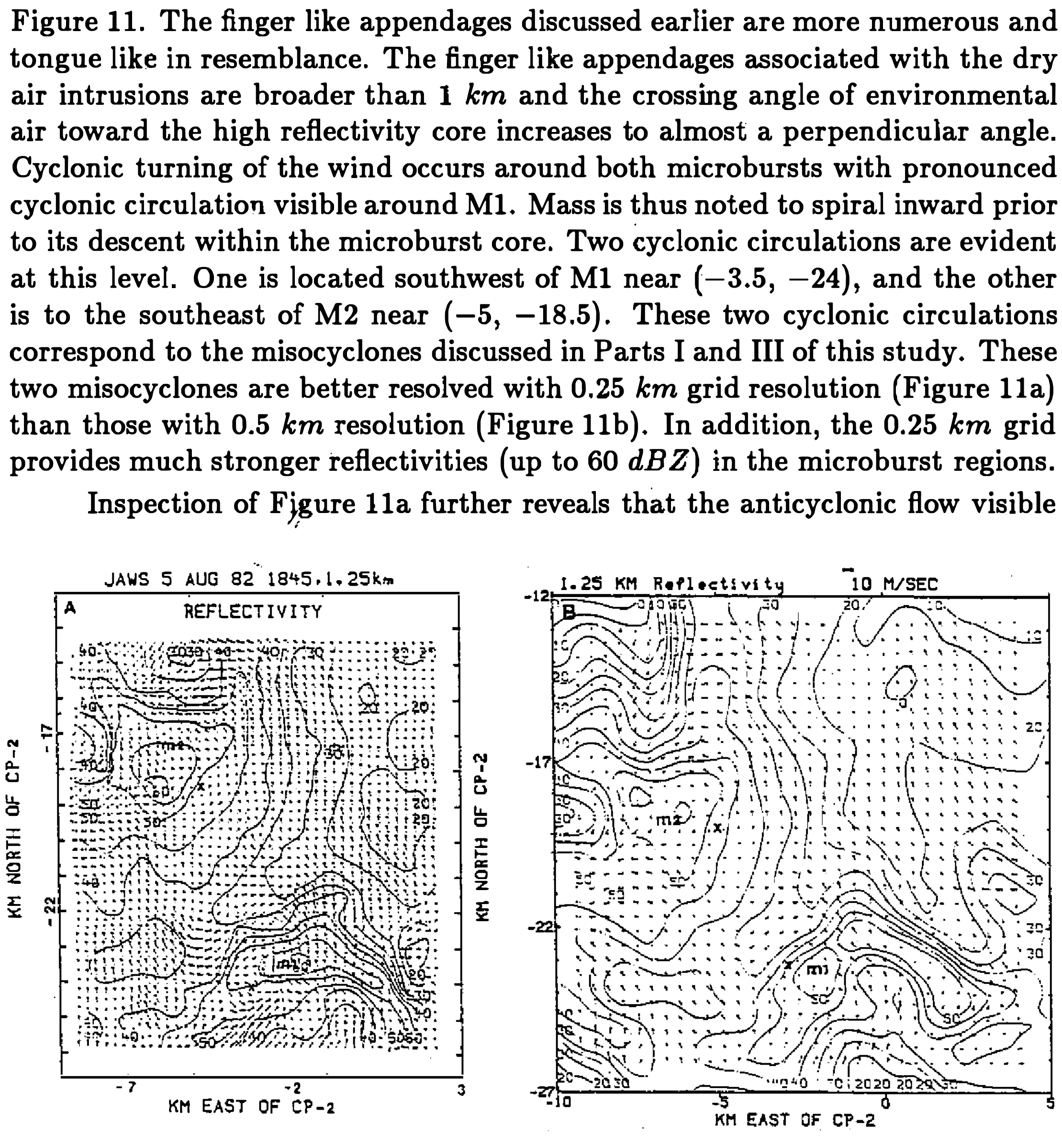

Fig. 11. As in Figure 1 except for 1.25 *km* AGL. A cross (x) signifies the center of misocyclone circulation.

to the southeast of the domain near (1, −24) is more pronounced than at 1 *km* and corresponds to the low-level cyclone attached to the southern flank of the surface gust front. A divergence of flow occurs on the southern flowing branch of M1's cyclonic circulation approximately 2 *km* west of its main core. The westward branch of this split flow feeds into anticyclonic curvature, while the eastern branch continues its cyclonic trek into the feeder tongue just south of M1. Mass inflow of dry air into M1 is from the southeast, while inflow for M2 occurs from the north. The strength of M1 both absorbs and seemingly blocks the environmental wind, thus forcing M2's circulation to draw its mass field from the north.

Unlike Fujita's (1985) description of the misocyclone structure, which described the misocyclone's role as one of a collector of hydrometeors for the microburst to enhance precipitation loading, Lin *et al.* (1991) proposed that the misocyclones act as pinwheels, which funnel in and efficiently channel dry environmental air for the enhancement of evaporative cooling by ventilating the saturated downdraft. Entrained air is mixed within the downdraft creating evaporative cooling which aids the development of negative buoyancy production. Conclusively, circulation enhancement spawned by the misocyclones aids to strengthen microburst affects launched at lower levels.

4.6 Vertical Cross Section

Figure 12 displays the west-east cross section of the wind field with reflectivity contours superimposed for both 0.25 and 0.5 *km* grid spacings. This cross

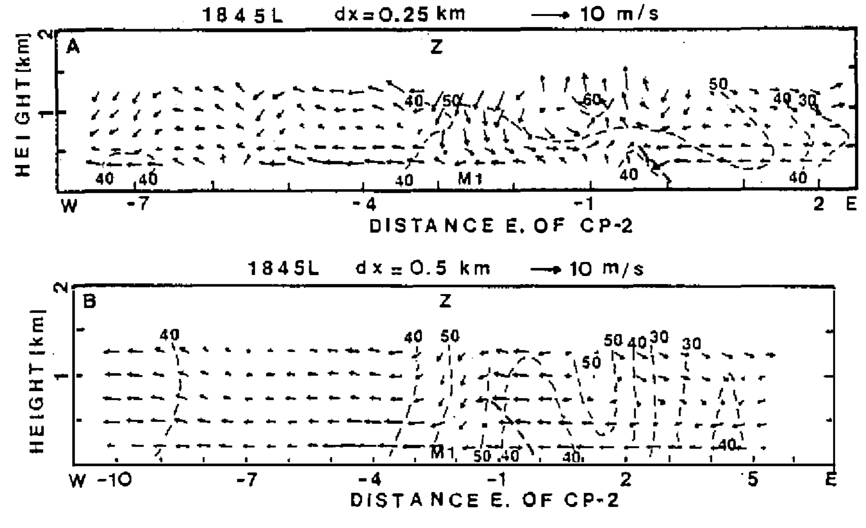

Fig. 12. The west-east cross section 23 *km* north of CP-2 showing the wind field with reflectivity contours superimposed for 1845 MDT 5 August 1982 using (a) 0.25 and (b) 0.5 *km* grid spacing. This cross section passes through the center of microburst M1. Contour interval is 10 *dBZ*. The dashed line denotes a microburst gurst front.

section passes through the center of microburst M1. Examination of Figure 12 shows that features revealed by 0.25 *km* resolution (Figure 12a) compare well with those by 0.5 *km* resolution (Figure 12b). Notice that M1 is located in the downdraft column with high reflectivities. It is accompanied by the updraft to its east in the vicinity of a microburst gust front (heavy dashed line). For 0.5 *km* grid analysis (Figure 12b), the air flow is generally from right (east) to left (west), but the 0.25 *km* grid datum (Figure 12a) reveals a more perturbed field of eddy motion within and around microburst M1.

Spatial variations of vertical velocity (w) along the same cross section for both 0.25 and 0.5 *km* spacings are presented in Figure 13. It is seen that microburst M1 maintains a maximum downdraft speed of $-6\ m\ s^{-1}$ with corresponding updraft speeds of $2 \sim 4\ m\ s^{-1}$ 1 *km* to its east near the gust front (Figure 13a). The maximum downdraft speed is about two times larger than that with 0.5 *km* resolution (Figure 13b). As noted earlier, the smaller grid spacing (0.25 *km*) can resolve fine-scale mesoscale features associated with microbursts. As a result, much larger values of the updraft and downdraft are discerned. Figure 13 clearly shows that the 0.25 *km* analysis datum depicts microburst features much more vividly and with larger values than those obtained at the 0.5 *km* analysis. Thus, the vertical velocity display for 0.25 *km* analysis

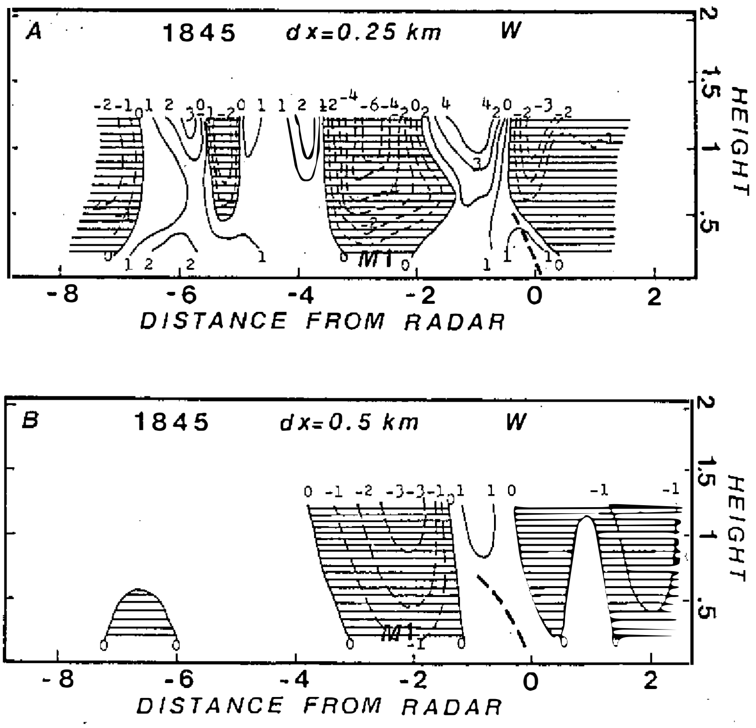

Fig. 13. As in Figure 12 except for vertical velocity. contour interval is $1\ m\ s^{-1}$. Negative values are shaded.

(Figure 13a) exhibits the overall storm intensity two to three times greater than those for 0.5 *km* analysis (Figure 13b).

Figure 14 displays the distributions of deviation perturbation pressure (Figure 14a) and temperature (Figure 14b) for the 0.25 *km* grid analysis. In the lowest layer near the surface, high pressure forms within the microburst inner core with low pressure to its right (east) and left (west). As a result, strong horizontal pressure gradients develop from the center of M1 toward the east and west. Such pressure gradients are necessary to accelerate the diverging outflow from the microburst inner core. These findings are consistent with those for the 0.5 *km* grid analysis (not shown) except the magnitude is somewhat larger. In the microburst-dominant region, relative cooling (up to $-3°C$) prevails at low levels. As discussed in Part I of this study, such cooling is mainly caused by evaporation of rain drops embedded within the downdraft column of air. As a result, a diverging outflow from the microburst center is negatively buoyant at low levels. On the east side of a microburst gust front (heavy dashed line), relative warming occurs. Such warming is associated with the incoming environmental air from the east, which is warmer than the microburst outflow at low levels. A distinct temperature contrast is evident across the gust front

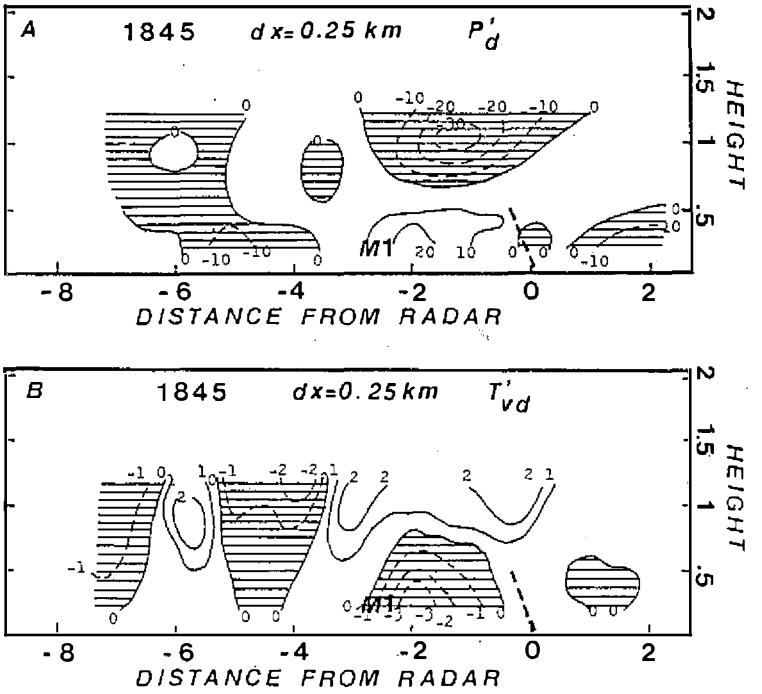

Fig. 14. The west-east cross section similar to Figure 12 showing (a) deviation perturbation pressure (P'_d) and (b) deviation perturbation temperature (T'_{vd}) with 0.25 *km* grid resolution. Contour intervals for P'_d and T'_{vd} are 10 *Pa* (0.1 *mb*) and 1°c, respectively. Negative values are shaded.

with warming on its east and cooling on its west. These features are in good agreement with those obtained by using 0.5 *km* grid spacing (not shown).

Based on the results presented above, we found that analyses with different grid resolution have revealed the delicate nature of microburst phenomena. In particular, the 0.25 *km* grid analysis often provides better resolution of those relevant features of microbursts as compared to those with 0.5 *km* resolution. As noted earlier, the 0.25 *km* grid analysis can resolve mesoscale feature with wavelength > 1.5 *km*, while the 0.5 *km* analysis can only resolve those with wavelength > 3 *km*.

5. CONCLUSIONS

Case studies of microburst-producing storms, conducted in Parts I and II of this study, have established the diversity of the microburst phenomena and the role played by the misocyclone with each individual storm. With the aid of 0.25 *km* grid spacing, we reexamined the 5 August 1982 case at 1845 MDT. Results show that structural features of a microburst-producing storm become more visible and readily identifiable. In particular, vertical velocities increase $2 \sim 3$ times at the 0.25 *km* grid analysis than those with 0.5 *km* resolution. However, the overall pattern of vertical velocity between the two analyses remains essentially the same. Magnitudes of deviation perturbation pressure and temperature for the 0.25 *km* analysis are found to be somewhat larger than those for the 0.5 *km* analysis. However, the differences are relatively small compared to those for vertical velocity mentioned early.

Examination of both analysis data sets has provided useful knowledge toward understanding the phenomena of a microburst-producing storm in the ABL. It was discovered that several features undetected at the 0.5 *km* grid spacing became vividly apparent at the 0.25 *km* grid datum. Furthermore, most features found became strikingly more apparent, both in magnitude and appearance than those reported in Part I of this study. When the data quality and resolution are adequate, a thermodynamic retrieval method can be employed to study some fine-scale structures of mesoscale disturbances in the ABL, including three-dimensional winds, pressure and temperature perturbations within a convective system, with success.

Acknowledgements. The authors wish to thank the National Center for Atmospheric Research (NCAR) for providing the dual-Doppler data and technical assistance. We are grateful to John Coover, Paul Lapointe and William McNamee for their help throughout the course of this study. This research was partially supported by the Division of Atmospheric Sciences, National Science Foundation, under Grant ATM-8312172-01. B. T. Regan was supported by the Air Force Institute of Technology.

REFERENCES

Armijo, L., 1969: A theory for the determination of wind and precipitation velocities with dual-Doppler radars, *J. Atmos. Sci.*, **26**, 570–573.

Barnes, S., 1973: Mesoscale objective analysis using weighted time series observations, *NOAA Tech Memo. ERL-NSSL-62*, 60 pp. (Available from National Severe Storms Laboratory, Norman, OK, 73069).

Cressman, G. P., 1959: An operational objective analysis system. *Mon. Wea. Rev.*, **87**, 367–374.

Elmore, K. L., J. McCarthy, W. Frost and H. P. Chang, 1986: A high resolution spatial and temporal multiple Doppler analysis of a microburst and its application to aircraft flight simulation, *J. Climate Appl. Meteor.*, **25**, 1398–1425.

Fujita, T. T., 1985: *The downburst microburst and macroburst*, University of Chicago Press, Chicago, 122 pp.

Gal-Chen, T., 1978: A method for the initialization of the anelastic equations: Implications for matching models with observations, *Mon. Wea. Rev.*, **106**, 587–606.

Hjelmfelt, M. R., 1988: Structure and life cycle of microburst outflows observed in Colorado, *J. Appl. Meteor.*, **27**, 900–927.

Kessinger, C. J., D. B. Parsons, and J. W. Wilson, 1988: Observations of a storm containing misocyclones, downbursts, and horizontal vortex circulation, *Mon. Wea. Rev.*, **116**, 1959–1982.

Koch, S. E., M. Des Jadins, and P. J. Kocin, An interactive Barnes objective map analysis scheme for use with satellite and conventional data. *J. Climate Appl. Meteor.*, **22**, 1487–1503.

Lee, W. C., R. E. Carbone, and R. M. Wakimoto, 1988: The evolution of a bow echo/microburst event in JAWS, Preprints, 15th Conference on Severe Local Storms, Baltimore, *Amer. Meteor. Soc.*, 391–394.

Lin, Y. J., W. E. McNamee, and J. A. Coover, 1991: Observational study of a multiple microburst-producing storm. Part I: Kinematic, dynamic, and thermodynamic structures. To appear in TAO.

Lin, Y. J., J. A. Coover, 1991: Observational study of a multiple microburst-producing storm. Part II: A comparison between the simple case and the complex case. To appear in TAO.

Lin, Y. J., P. G. Lapointe, 1991: Observational study of a multiple miroburst-producing storm. Part III: Vorticity budgets. To appear in TAO.

Wilson, J. W., R. D. Roberts, C. Kessinger, and J. McCarthy, 1984: Microburst wind structure and evaluation of Doppler radar for airport wind shear detection, *J. Climate Appl. Meteorol.*, **23**, 898–915.

產生微爆雷雨系統之觀測研究
（四）細尺度分析

林永哲 Bradley T. Regan Robert W. Pasken
美國聖路易大學地球與大氣科學系
美國空軍氣象勤務中心

摘要

本文使用的觀測資料是發生於1982年8月5日18:45（LST）的數個微爆個案。配合JAWS計劃，使用雙都普勒雷達觀測這幾個暴風雨的動能場，動力場，熱力場，以網格距0.25km的客觀分析方法，計算出相對暴風雨之風速以及回波值，並與先前網格距0.5km之研究比較。垂直方向由0.25km至1.25km分爲五層。垂直速度是以非彈性連續方程式，由地表向上積分至邊界層頂。並使用熱力反求法，從以三動量方程式計算出的都普勒風場反推算出壓力與溫度擾動場。

結果顯示：以0.5km爲網格尺度所無法見到的某些現象，在0.25km網格尺度下，非常明顯。更甚者，在此次研究中見到的大部份現象，無論在尺度或外觀上，都令人訝異地遠比前一個使用0.5km格距時明顯。以雙都普勒雷達計算出的風場的品質與解析度，直接決定了熱力反求技術的成功與否。